Journal of Physics D:
Applied Physics

Temporal dynamics of TiO$_x$ memristor for reservoir computing applications

To cite this article: Alexander-Hanyu Wang *et al* 2026 *J. Phys. D: Appl. Phys.* **59** 015101

Journal of Physics D: Applied Physics

OPEN ACCESS

RECEIVED
30 July 2025

REVISED
24 October 2025

ACCEPTED FOR PUBLICATION
25 November 2025

PUBLISHED
24 December 2025

PAPER

Temporal dynamics of TiO_x memristor for reservoir computing applications

Alexander-Hanyu Wang[*], **Xiyue Fan**, **Zixuan Zhang**, **Omesh Kapur**, **Ruomeng Huang**[*], **Firman Simanjuntak**, **Harold M H Chong** and **David B Thomas**

School of Electronics & Computer Science, University of Southampton, Southampton SO17 1BJ, United Kingdom

[*] Authors to whom any correspondence should be addressed.

E-mail: a.wang@soton.ac.uk and r.huang@soton.ac.uk

Keywords: reservoir computing, memristor, short-term plasticity, read timing, variation

Supplementary material for this article is available online

Abstract

The growing computational demands of artificial intelligence have accelerated the development of energy-efficient neuromorphic systems capable of processing spatiotemporal information. Reservoir computing (RC) offers a promising approach with low training complexity, particularly when implemented using emerging devices such as memristors. In this work, we present a memristor-based RC system employing vertically stacked Pt/TiO_x/Au volatile memristors that inherently exhibit short-term plasticity. These devices enable temporal information encoding via pulse-driven modulation and natural relaxation. Through a modified MNIST classification task, we demonstrate that the system performance deteriorates significantly with delayed readout and small levels of device variation, highlighting the need for robust timing strategies. A virtual memristor model was also developed to evaluate system performance on the Mackey-Glass chaotic time-series forecasting task, achieving up to 93.6% prediction accuracy by tuning the internal time constant. These findings highlight the importance of precise readout control and variation resilience in the design of practical memristor-based RC systems for real-world neuromorphic applications.

1. Introduction

The surging demand for artificial intelligence (AI) application, ranging from speech recognition to time-series forecasting, has increasingly relied on vast computational resources [1–4]. The traditional von Neumann computing architecture struggles to meet the computational and energy requirements of modern AI workloads, creating an urgent need for alternative paradigms that can process complex data with lower power consumption [5, 6]. Neuromorphic computing, which draws inspiration from the highly efficient biological brain, offers a compelling alternative [7]. Operating at just ∼20 W, the human brain excels at parallel information processing and time-dependent tasks, owing to its intricate synaptic dynamics and non-linear behaviour. Unlike conventional computers, the brain performs computation and stores memory within the same neural structures, allowing for highly efficient and integrated information processing [8]. As a result, neuromorphic computing seeks to replicate these principles, aiming for systems that are both energy-efficient and capable of sophisticated, brain-like computation.

Among various neuromorphic approaches, Reservoir computing (RC), a specialised form of recurrent neural networks, has emerged as a particularly promising method especially for processing temporal data with reduced training complexity [9, 10]. RC employs a fixed, randomly interconnected reservoir layer that nonlinearly transforms input signals into a high-dimensional state space [11–14]. Only the output layer undergoes training, significantly reducing computational overhead while maintaining competitive accuracy in processing complex spatio-temporal data [15, 16]. Additionally, this approach promotes efficient learning and enables the use of various dynamical systems as reservoirs, making RC highly adaptable to a wide range of tasks with minimal parameter tuning [17, 18]. The key to the RC system is its reservoir, which acts as a nonlinear transformation layer that projects input signals into a high-dimensional space, allowing one-layer feature extraction therefore reducing training cost. Different types of hardware, ranging from traditional transistor-based circuits to spintronic systems, have been explored as the reservoir layer in the RC systems [19, 20]. However, the complexity of implementing these hardware solutions and difficulties in achieving robust nonlinear dynamics have driven the search for alternative platforms that can naturally emulate the non-linear dynamics and memory retention features of biological synapses.

Two-terminal memristors have emerged as a compelling solution as they offer compactness, nonlinearity, and memory retention that closely parallel synaptic functions in the brain [7]. Memristors can be classified as non-volatile or volatile, analogous to long-term and short-term memory (STM) in biological systems [21]. Non-volatile memristors retain their state for extended periods, while volatile memristors revert to their original state shortly after stimulus removal, with the transition timescales tuneable by material and device parameters [21–25]. This volatility makes them particularly suitable for the reservoir layer, where their nonlinear, dynamic responses can be effectively harnessed to build energy-efficient, scalable, and hardware-accelerated RC systems. Many volatile memristors based on different materials including ZnO_x, WO_x, SiC and nanoporous silica have been explored as reservoir layer in RC computing system [26–29]. Among the various memristive materials explored, titanium oxide (TiO_x) has emerged as a leading candidate due to its reliable switching behaviour, excellent material stability, and seamless compatibility with CMOS fabrication processes [26, 30–32]. TiO_x memristors have been shown to effectively emulate synaptic characteristics, including both potentiation and depression characteristics through pulse modulation, making them particularly well-suited for implementation in RC systems [33, 34]. The temporal dynamics of TiO_x-based memristors have been well-documented in the literature. In particular, synaptic depression has been observed on timescales ranging from microseconds to milliseconds. This behaviour provides key neuromorphic computing features, such as learning, forgetting, and spike-timing-dependent plasticity [35–37]. The TiO_x-based memristors have been implemented in applications such as visual pattern recognition, tactile sensing and electrocardiogram analysis [38–40].

Despite the expanding body of research in memristor-based RC, a critical gap persists in understanding and optimising the temporal dynamics of volatile memristors. Since these dynamics involve the evolution of their current state over time, along with the associated rate of change governed by the time constant. The role of precise readout timing plays a critical role in overall system performance, since the information encoded in volatile memristors weakens over time. However, no prior work has quantified this effect by exploring the optimal readout point or the extent to which this information is retained. Furthermore, the data retention window of volatile memristors could potentially serve as a sampling window in field programmable gate arrays (FPGAs), removing the requirement for exact clock synchronisation without the need for additional resources or introduced delays. Such approach might offer a promising pathway to address existing FPGA challenges, including the extensive time and computational resources required by machine learning-assisted synthesis to achieve timing convergence, such as timing closure and rectifying timing violations as described by Taj and Faroo [41]. Additionally, while previous studies have demonstrated the feasibility of using memristive devices in RC architectures, the timing sensitivity of volatile memristors is frequently overlooked, despite its clear relevance to both memory retention and noise robustness in spatio-temporal tasks.

In this work, we address the optimal read timing and its effects on the system accuracy by systematically investigating the role of timing dynamics in TiO_x-based volatile memristors for RC. We first characterise how input parameters (voltage, pulse width, and interval) modulate short-term potentiation (STP) and short-term depression (STD) rates, establishing design guidelines for optimal reservoir operation. Secondly, using the MNIST dataset, we then demonstrate that the accuracy of image recognition tasks is highly sensitive to the final readout timing, revealing that misalignment between the read timing and the memristor's state decay can significantly degrade the computational performance. Furthermore, we quantify the system's resilience to input noise variation and evaluate the retention window during which encoded information remains viable for processing. Finally, we translate experimental observations into a digital twin model that accurately replicates STP and STD dynamics, validating its utility in time-series forecasting tasks via the Mackey–Glass (MG) benchmark.

2. Experimental methods

This section details the experimental methods employed in fabrication and characterisation of the TiO_x-based volatile memristors, as well as the computational evaluations in RC applications. We begin with establishing a baseline for memristive behaviour, following by assessments using the MNIST dataset for pattern recognition and the MG system for time-series prediction.

2.1. Device fabrication and characterisation

Vertically stacked Pt/TiO_x/Au crosspoint memristors were fabricated on a SiO_2/Si substrate. The Au bottom electrode (20 nm) with a 5 nm Ti adhesion layer were deposited by e-beam evaporation (Leybold Lab 700). The TiO_x dielectric layer (25 nm) was deposited using reactive magnetron sputtering (Leybold Helios ProXL), with 8 sccm O_2 and 25 sccm Ar flow rate. The Pt top electrode (15 nm) was subsequently fabricated also via sputtering process. The patterning of the crosspoint arrays was achieved through a series of lithography processes and the dimension of each memristor was defined by the overlapping area of the crossed bars. The area of the memristor devices used in this work is $35\ \times 35\ \mu m^2$.

X-ray photoelectron spectroscopy (XPS) measurements were performed using a Theta Probe System with an Al Kα source (photon energy = 1486.6 eV). All the binding energies were calibrated with respect to the peak of the adventitious C−C peak at 284.8 eV. Electrical characterisations were performed using a Keysight B1500A device parameter analyser, integrated with a B1530A waveform generator. All test devices were individually connected with dedicated pads for probe connections. During the measurement, a voltage bias applied to the top electrode, while the bottom electrode was grounded. Read measurements were taken exclusively from the top electrode to ensure a more accurate representation of the device state. A custom designed probe card was used to map the column and row contact pads to the corresponding devices in a cross-shaped arrangement. This connected all 32 devices simultaneously to the Keysight 34 980 A data acquisition matrix, which is operated by a custom script that provided the interface to select any device for characterisation.

2.2. MNIST pattern recognition

To assess physical volatile memristors within a RC framework, the MNIST dataset of 28×28 grayscale handwritten digit images $(0-9)$ was used to test the system's performance. The images were binarised using a fixed threshold of 100/255 to produce binary values for emulating the distinct current states of the memristor. The preprocessing utilised a small training set of 10 000 MNIST images as an input to simulate RC system, with binary patterns mapped to the memristor current responses. Binarised images were converted into sequence of current values that represents the current states. To account for hardware variability, Gaussian noise variation of up to 5% was applied. Feature vectors were split into training, validation and test sets of 80%, 10% and 10% respectively. A feedforward neural network with a SoftMax-activated output layer was trained for ten-class classification. System performance was evaluated through test accuracy across varying levels of CoV. Further details of the MNIST training and associated training loss curves can be found in section 1 in the Supporting Information.

2.3. Mackey-glass system prediction

The MG system is a well-established benchmark for evaluating chaotic time-series prediction to model nonlinear processes through delayed feedback mechanisms. The dynamics of the MG system are governed by the following delay differential equation [42]:

$$\frac{\mathrm{d}x}{\mathrm{d}t} = \beta \frac{x(t-\tau_0)}{1+x(t-\tau_0))^n} - \gamma x(t)\,.$$

In this context, represents the state of the system at time t, τ_0 is the delay time, β and γ define the growth and decay rates of the system, respectively, and n controls the non-linearity of the feedback. To evaluate the predictive capability of the proposed memristor-based RC framework, the MG system was simulated using standardised chaotic parameters: $\beta = 0.2$, $\gamma = 0.1$, $n = 10$, and $\tau_0 = 17$ [43]. A raw dataset of 3000 data points was generated using the MG equation. Every third data point was sampled to reduce temporal redundancy, yielding a final dataset that was evenly split into training and test sets. A memristor-based model, parameterised using experimental data (detailed in section 2 of the supporting information), was implemented to simulate the dynamic behaviour of the volatile TiO_x devices.

The RC system was configured as a simulated parallel architecture, utilising 10 virtual memristor nodes modelled after the experimental TiO_x devices, thereby improving computational efficiency through parallel processing of the time-series data across the nodes. For each prediction instance, the input consisted of 10 previous x–values, with the corresponding target output being the next y-value—thus establishing a time-lagged prediction framework. Each of the 10 virtual memristor nodes processed the same input sequence using a unique transformation mask derived from a $10\ \times\ 10$ mask matrix. This configuration enabled the generation of a total of 1000 distinct reservoir states, each reflecting varied dynamic transformations of the input data. To ensure model robustness, a 10-fold cross-validation strategy was used on the training dataset to identify optimal hyperparameters for ridge regression. Prior to readout, a scalar multiplier was applied to normalise the reservoir states, preventing numerical instability due to excessively large or small values. The readout layer employed ridge regression to establish a robust mapping between the transformed reservoir states and the desired output values, mitigating overfitting and improving generalisation. The reservoir states were arranged sequentially to form a comprehensive input matrix, which was then supplied to the readout layer therefore permitting the RC system to integrate the diverse transformations into a unified prediction result.

3. Results and discussion

The key experimental results from the characterisation of TiO_x-based volatile memristors and their application in RC tasks are presented below, focusing on their influence on volatile characteristics and examining the impact of timing dynamics on system performance and optimisation.

3.1. TiO_x material characterisation

Figure 1(a) illustrates a photograph of the fabricated Pt/TiO_x/Au crosspoint memristor arrays on a 6-inch silicon wafer. Each array consists of 32 individual memristor cells, as illustrated in the optical microscope image shown in figure 1(b). To analyse the chemical composition and oxidation states within the TiO_x dielectric layer, XPS was performed. The survey spectrum in figure 1(c) confirms the presence of both Ti and O peaks, with no visible impurities, consistent with findings reported in [44]. Detailed analysis of the Ti 2p core-level spectrum, shown in figure 1(d), reveals two distinct sets of Ti $2p_{3/2}$ and Ti $2p_{1/2}$ spin-orbit doublets. The peaks at 459.0 eV and 465.0 eV are attributed to the $Ti^{4}+$ oxidation state, characteristic of TiO_2 [45, 46], while the peaks at 457.1 eV and 463.1 eV correspond to the $Ti^{3}+$ state, typically associated with Ti_2O_3 [47, 48]. This coexistence of $Ti^{4}+$ and $Ti^{3}+$ oxidation states suggests that the TiO_x film is composed of a mixed-phase matrix of TiO_2 and Ti_2O_3. The O 1s core-level spectrum, shown in figure 1(e), further supports this finding. Two prominent peaks are observed at 530.4 eV and 531.3 eV, corresponding to oxygen bonded in TiO_2 and Ti_2O_3, respectively [46, 48]. Quantitative analysis yields a Ti:O atomic ratio of approximately 1:1.78, which deviates from the stoichiometric ratio of TiO_2 (1:2), indicating a significant level of oxygen deficiency within the film. Such high oxygen vacancy level is known to result in increased concentrations of oxygen vacancies, which can contribute to higher leakage currents and reduced retention stability, characteristics commonly associated with STM behaviour. The implications of this on device performance are examined in detail in the following section.

3.2. Synaptic switching of TiO_x memristor

Figure 2(a) presents a schematic illustration of the Pt/TiO_x/Au memristor used in this study, specifically engineered to emulate brain-like functionality by replicating key synaptic behaviours. The synaptic response to the stimulation of a series of electrical pulses is shown in figure 2(b). The stimulation pulse consists of a series of 200 pulses (4 V), each with a duration of 100 μs and interval of 8 μs. The synaptic weight, which is defined as the memristor current, is collected at a read voltage of 0.1 V after each pulse. It can be observed that the currents gradually increase upon the application of electrical pulses, reflecting a facilitation effect. Following the withdrawal of stimulation, the current decays into its initial current state automatically, demonstrating a typical short-term plasticity behaviour which is crucial for application in spatiotemporal information processing. It is worth noting that such STP behaviour is observed in pristine devices without the need for any electroforming or pre-conditioning processes. This intrinsic response simplifies device operation and is beneficial for the integration in neuromorphic hardware. This STP behaviour observed in our TiO_x-based memristors is likely attributed to the high concentration of oxygen vacancies within the dielectric layer. Under the application of positive voltage pulses, these vacancies are mobilised, forming transient conductive pathways that result in a gradual increase in device current. However, in the absence of continued stimulation, these pathways are inherently unstable. The spontaneous relaxation of charge carriers and the thermodynamic re-distribution of oxygen vacancies toward their equilibrium state lead to a natural decay of the current, thereby producing the characteristic STP response [49]. Similar STP behaviours were also observed in other oxygen-deficient memristor devices [37, 50, 51].

The observed STP behaviour is sensitive to temporal parameters and can be modulated by varying the input pulse conditions. Figure 2(c) presents the potentiation responses of the memristor when subjected to pulse trains with fixed voltage (4 V) and duration (100 μs), while the inter-pulse interval was systematically varied from 8 μs to 1024 μs. It is observed that smaller pulse interval results in a greater change in current, especially within the first pulse, indicative of enhanced synaptic facilitation. This behaviour represents the typical spike-rate-dependent-plasticity (SRDP) where the frequency of input stimuli can influence the synaptic weight. Similarly, the effect of input amplitude on synaptic response is

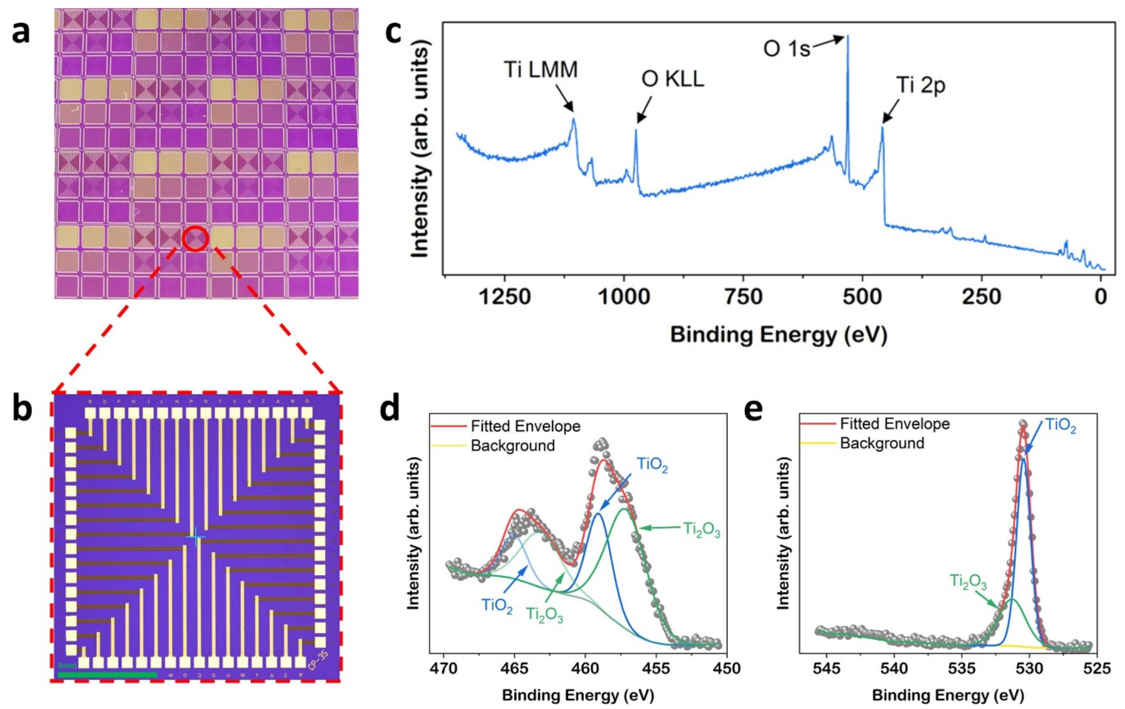

Figure 1. (a) Image of Pt/TiO$_x$/Au memristor crosspoint arrays fabricated in this work. (b) Optical microscope image of a Pt/TiO$_x$/Au cell consisting of 32 memristor devices. (c) XPS survey spectrum of the TiO$_x$ film. (d) XPS core level spectrum of Ti 2p. (e) XPS core level spectrum of O 1s.

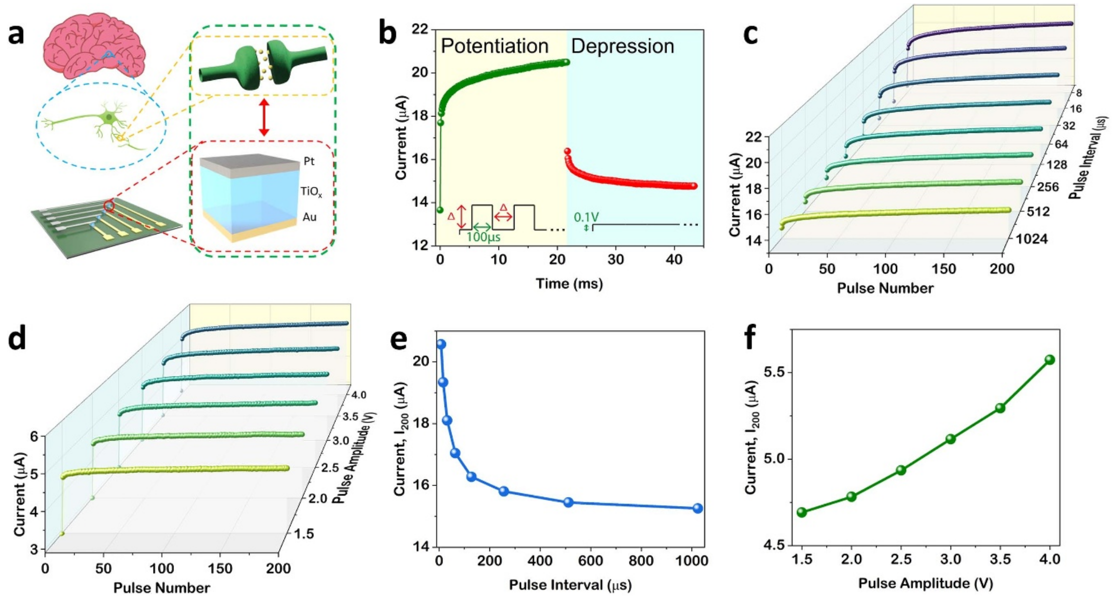

Figure 2. (a) Illustration of the Pt/TiO$_x$/Au memristor capable of mimicking synaptic behaviour in the brain. (b) Gradual current change of the Pt/TiO$_x$/Au memristor with a series of voltage pulses and the subsequent auto-decay showing the STP behaviour. (c) Current response of the device for pulses with fixed 4 V pulse amplitude and different pulse intervals, emulating SRDP behaviour. (d) Current response of the device for pulses with fixed 8 μs pulse interval and different pulse amplitudes, emulating SVDP behaviour. Final current state after 200 consecutive pulses under different (e) pulse intervals and (f) pulse amplitudes, respectively.

shown in figure 2(d). In this case, both the pulse width and interval were held constant at 100 μs and 8 us, while only the pulse amplitude was varied from 1.5 V to 4 V. As the pulse number increases, a continuous rise in current is still observed, indicating that subsequent pulses after the first one continue to influence the memristor's state. An increase in current response with higher input voltages is observed, demonstrating spike-voltage-dependent plasticity (SVDP). The final states after 200 consecutive pulses

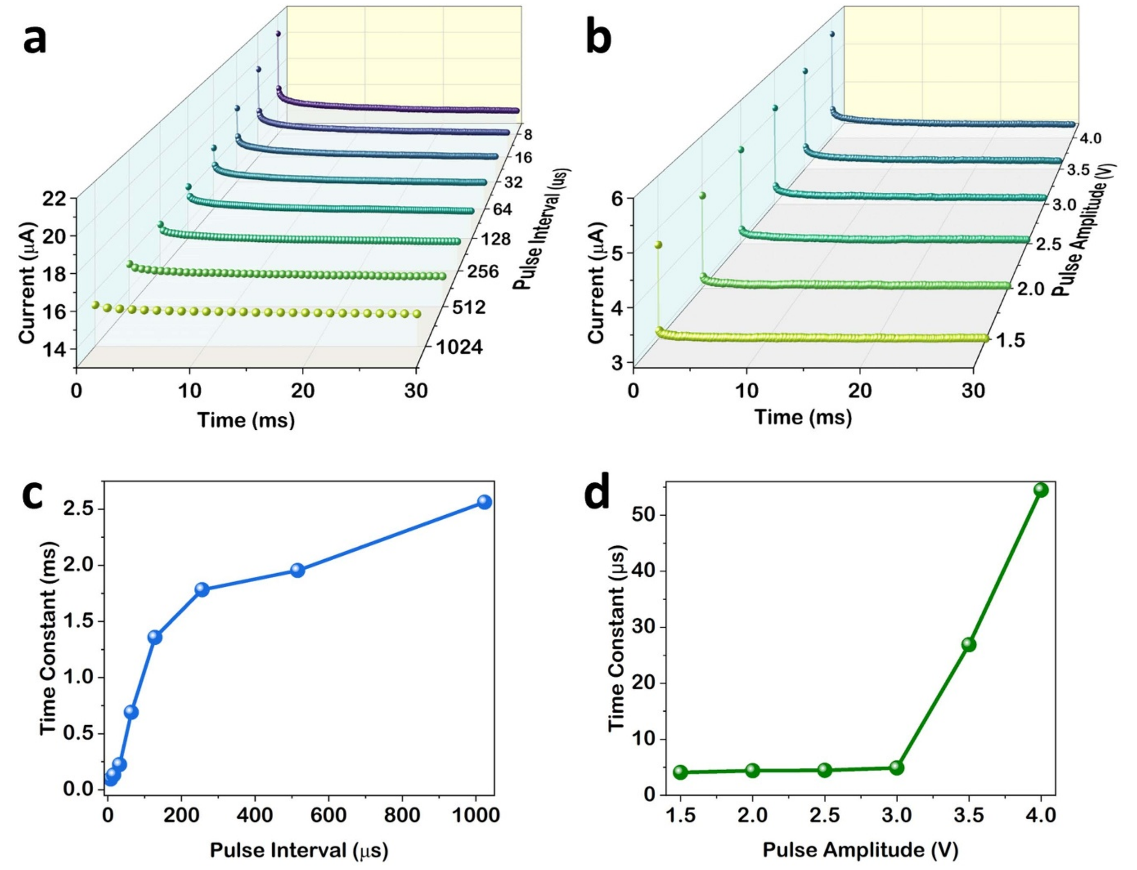

Figure 3. (a) 3D plot illustrating natural relaxation behaviour across different pulse intervals. (b) 3D plot depicting natural relaxation behaviour across different pulse amplitudes. (c) Calculated τ values for the natural relaxation period corresponding to each pulse interval. (d) Calculated τ values for the natural relaxation period corresponding to each varying pulse amplitude.

based on SRDP are shown in figure 2(e). Higher-frequency SRDP provides a larger dynamic range compared to lower frequencies with longer pulse intervals. Similarly, figure 2(f) demonstrates that altering the pulse amplitude of individual pulses produces a greater dynamic range and higher final state.

Figures 3(a) and (b) plot the spontaneous decay processes after applying the pulses with different intervals and amplitudes. The rate of decay is influenced by the input signal and the intensity of the pulses. Under natural exponential decay with 0.1 V read pulses at varying intervals shows that higher pulse frequency (or shorter pulse intervals) triggers a larger reduction in current in comparison to lower pulse frequency. A similar pattern is observed based on a range of input pulse amplitudes where larger amplitude produced a more significant current decrease. Most of the decay occurs within the first 5ms for both types of inputs, whether varying the pulse interval or the amplitude. The relaxation curves for amplitude variations were fitted using the first 50 data points during the relaxation period. Varying the pulse interval increases the time constant value, τ, with longer pulse intervals producing the longest time to reduce by $1-1/e \approx 63.2\%$ of the final state, as shown in figure 3(c). Similarly, modulating the pulse amplitude results in an increase in the time constant value from 3.0 V to 4.0 V with 4.0 V requiring the longest time to reach τ state, thereby a larger dynamic range to travel through, as shown in figure 3(d). The increase in the time constant with larger pulse intervals or higher pulse amplitudes can be attributed to the prolonged influence of the input signal on the device's oxygen ion dynamics. Longer pulse intervals, corresponding to lower stimulation frequencies, reduce the cumulative effect on the device that results in smaller deviation from the HRS equilibrium state and increased difficulty for the decay. In contrast, shorter pulse intervals drive a faster decay rate, which prevents significant stabilisation and keeps a less stable state. Higher pulse amplitudes deliver greater energy, intensifying the relaxation dynamics, which requires longer to reduce by 63.2% of the final state.

3.3. Programming and relaxation states

The unique STP property of our TiO_x memristor enables its capacity to discriminate between input sequences with different temporal orders. To demonstrate this capability, the device was stimulated with

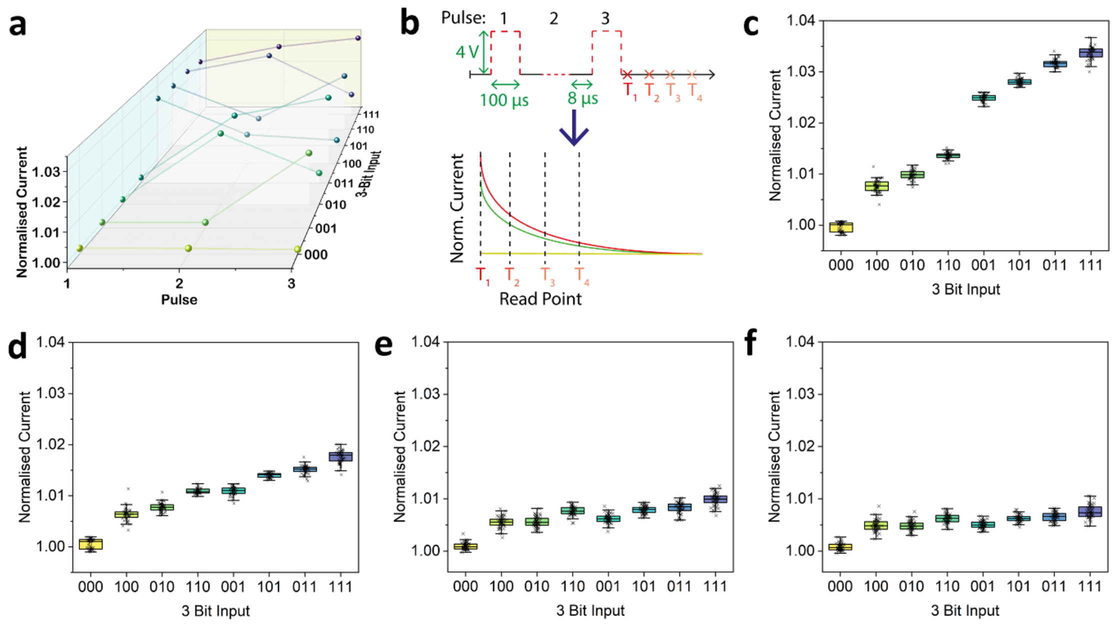

Figure 4. (a) The state of the device after each individual pulse as part of the 3-bit experiment. (b) Illustration showing recorded current state at the specified read timings, in this example, a '101' input is shown followed by decay. Box plot demonstrating the distribution and variability of the normalised current for each input measured at the reading point of (c) T_1, (d) T_2, (e) T_3, and (f) T_4.

a series of pulse trains, each comprising three binary pulse bits. This configuration allows for a total of eight unique input combinations (from '000' to '111'). Each bit was either a high-state pulse (4 V, denoted as '1') or a low-state pulse (0.1 V, denoted as '0'), with a fixed duration of 100 μs and an inter-pulse interval of 8 μs. Figure 4(a) presents the current state throughout each unique pulse train. Due to the nature of the volatile behaviour, increase and decrease in current can be observed during programming. Figure 4(b) illustrates an example of a '101' pulse train and four read timings after programming. To investigate the impact of read timing, we recorded the resultant current at four read time points, designated T_1, T_2, and T_4 —occurring at 0 μs, 108 μs, 648 μs and 1728 μs after the final input pulse. Figure 4(c) plots the current outputs for all 8 states when measured at T_1. The results show distinct current levels for each pattern, confirming the memristor's ability to differentiate sequences based on temporal order. This discriminative capability is particularly advantageous for spatiotemporal information encoding in RC frameworks. The error bars shown represent cycle-to-cycle (C2C) variation, with each input sequence repeated 50 times to assess statistical stability. Despite inherent variability, the output currents remain sufficiently distinguishable. However, as the readout is delayed, the distinct separation between current levels corresponding to different input sequences diminishes due to continued current decay within the memristor. This effect is illustrated in figure 4(d), which shows the output measured at read timing T_2. The reduced contrast in current levels reflects the progressive relaxation of the device's internal state over time. At later read timings T_3 and T_4, shown in figures 4(e) and (f) respectively, the differentiation between input patterns becomes increasingly limited. By T_4, the current responses converge to nearly indistinguishable values, indicating that the transient synaptic states have largely decayed. These observations underscore the critical importance of precise read timing. The ability to capture and utilise the encoded information depends heavily on when the read operation is performed relative to the input stimulus. This timing-dependent behaviour and its implications for RC system performance are further explored in the following section.

3.4. MNIST image recognition

The RC system offers an ideal framework for incorporating the volatile behaviour of memristors as nodes within the reservoir. This approach uses the dynamic state changes of memristors as shown in figure 5(a), where input signals with fixed weights (W_{in}) are processed through the reservoir then mapped to output signal with trained weights (W_{out}). To implement memristor-based RC using experimental data, images from the MNIST grayscale digit database were first pre-processed. The grayscale

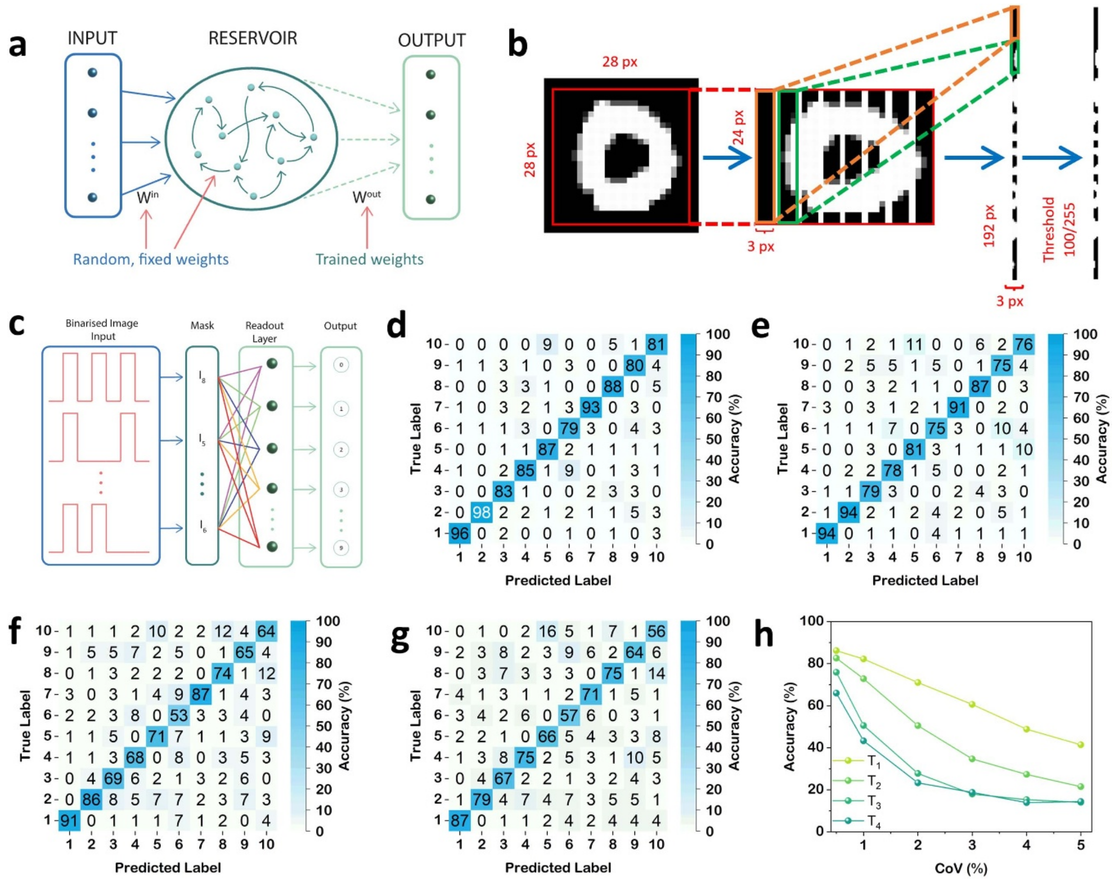

Figure 5. (a) Illustration of the RC system, where the input and reservoir layers utilise fixed weights, and only the output layer is trained to minimise computational load. (b) The MNIST images were first divided and then rearranged into a 3 × 192 pixel arrangement for training. (c) Illustration of the data processing flow within a RC system where binary input values are mapped to the C2C mean values of the device output, which are subsequently used for training the readout layer in the RC framework. Confusion matrix of the true label against the predicted label with 0.5% CoV at read timing (d) T_1, (e) T_2, (f) T_3, and (g) T_4, respectively. (h) MNIST prediction accuracy at four read timings with varying CoV levels from 0.5% to 5%.

images were converted to binary format by applying a threshold value of 100 (on a scale of 0–255), assigning a value of ‘1’ to pixels darker than the threshold (black) and ‘0’ to brighter pixels (white). In addition, all MNIST image (28 × 28 pixels) were cropped to remove the outer 2-pixel border, yielding a central 24 × 24 pixel region to focus on the core digit structure. Each processed image was subsequently divided vertically into eight equal parts and recombined into a single 3 × 192-pixel vertical strip, as shown in figure 5(b). This restructuring is designed to aligns with the experimental input encoding scheme and facilitates efficient mapping of binary data to temporal memristor states, thereby enabling effective integration of the device’s dynamic behaviour into the RC system. This binary representation was then mapped to the experimentally achieved currents at different read timings T_n, which were used as input data for the feedforward readout network, as depicted in figure 5(c).

The MNIST classification task evaluates the impact of varied readout timings under a fixed relaxation time, focusing on the optimal sampling point. Specifically, how different delayed readout points, combined with noise variability, affect pattern recognition accuracy. The performance of the trained RC system based on our TiO_x memristors was evaluated by classifying digit patterns from an unseen test dataset under varying readout times and device variation conditions. Under ideal conditions with no variation (CoV = 0%), the RC system consistently achieved similar classification accuracies over 90% across all four readout times. This high performance is attributed to the distinct mean current levels associated with each 3-bit input, which remain separable even at later readout times. However, in practical implementations, memristor-based systems are inherently subject to both C2C and device-to-device (D2D) variations. Prior studies have reported such variations ranging from a few percent up to tens of percent [52–56], which can significantly compromise the stability and reliability of RC system performance. Additionally, state separability could be further enhanced by utilising memristors with more gradual decay characteristics, achieved either through larger input parameters to compensate for slower decay or by optimising material properties and device designs. This approach would extend the viable relaxation window and maintain distinguishable current levels over extended readout timings. However, such extensions are not always feasible without trade-offs, as they would limit the inherent volatility required for time-dependent signal processing capabilities in RC, potentially impacting switching speed, energy efficiency, or material stability. More importantly, memristors must possess diverse temporal characteristics to provide effective time-dependent signal processing. Input signals often feature multiple frequencies, demanding both rapid and gradual decay characteristics. Relying solely on gradual decay prevents the handling of complex, multi-frequency signals, therefore the use of a combination of rapid and slow response rates ensures flexible functionality [57].

To emulate realistic device behaviour under varying degrees of uncertainty, we applied controlled levels of variation to the average current values. This allowed for a more accurate evaluation of the RC system's robustness and tolerance to stochastic fluctuations. For each CoV level, noise was introduced by superimposing a Gaussian-distributed component onto the nominal current values, where the standard deviation was defined as a fraction of the mean current (i.e., proportional to the CoV). Figure 5(d) shows the resulting confusion matrix obtained using current values measured at read timing T_1 with 0.5% CoV, yielding an overall classification accuracy of 86.2%. This result demonstrates the system's ability to recognise spatiotemporal patterns under minor variability. The classification performance using current values measured at is presented in figure 5(e), with a reduced accuracy of 82.6% compared to T_1. As the read timing progressed, performance continued to decline, reaching 75.9% and 66.0% at T_3 and T_4, respectively (figures 5(f) and (g)). This decline reflects a progressive loss of separability among input states at later readouts. We further investigated the RC system performance across a range of CoV levels for all four read timings (figure 5(h)). Even small levels of variation led to noticeable drops in performance. For example at 1% CoV, classification accuracy deteriorated significantly at T_3 and T_4 (to 50.6% and 43.3%, respectively), where the current distributions had largely converged and become indistinguishable. This loss of separability directly impaired the RC system's ability to infer the correct input patterns. These findings underscore the critical importance of read timing in memristor-based RC systems. Precise timing is essential to preserve the distinguishability of transient synaptic states and to maintain high classification accuracy in spatiotemporal tasks. These results emphasise the need for carefully optimised readout strategies and variation-aware circuit design in practical memristor-based RC implementations.

3.5. Mackey-glass forecasting

The MG system is a widely utilised benchmark for evaluating time-series forecasting models, particularly in the context of RC frameworks [58, 59]. Due to its inherent nonlinearity and time-delayed dynamics, the MG system presents a meaningful challenge for predictive modelling, closely resembling the complexity of real-world chaotic systems. In comparison to the MNIST classification task, the MG prediction task assesses the role of the relaxation time constant in dynamic time-series forecasting. This was achieved through an implementation of a fixed readout point and adjusted the memristor's relaxation decay time constant within the device model to demonstrate effects of the 'forgetfulness' of the reservoir states, as illustrated in figure S6 of the supporting information. Figure 6(a) illustrates the performance of the virtual memristor-based RC system, showing a comparison between the predicted and actual MG time-series in the time domain. The corresponding predicted trajectory in phase space is shown in figure 6(b), offering a visual representation of the system's dynamic behaviour. Similar to variations in read timing, employing a shorter (i.e., more 'forgetful') time constant of 0.001 443 ms resulted in a prediction accuracy of 72.2%, evaluated within a ±5% tolerance band relative to the ground truth signal amplitude. Increasing the relaxation time constant to 0.014 43 ms improved the prediction accuracy to 87.9%, as shown in figure 6(c), with the corresponding phase space plot further confirming enhanced trajectory fidelity as shown in figure 6(d). A further increase to 1.44 ms in figure 6(e) led to an accuracy of 93.6%, with strong agreement between predicted and actual time series. The corresponding phase space in figure 6(f), demonstrates the RC system's ability to faithfully capture and reproduce the complex, nonlinear structure of the chaotic attractor. These results clearly demonstrate that tuning the internal temporal dynamics of memristor-based reservoirs—specifically through the relaxation time constant—significantly impacts prediction performance.

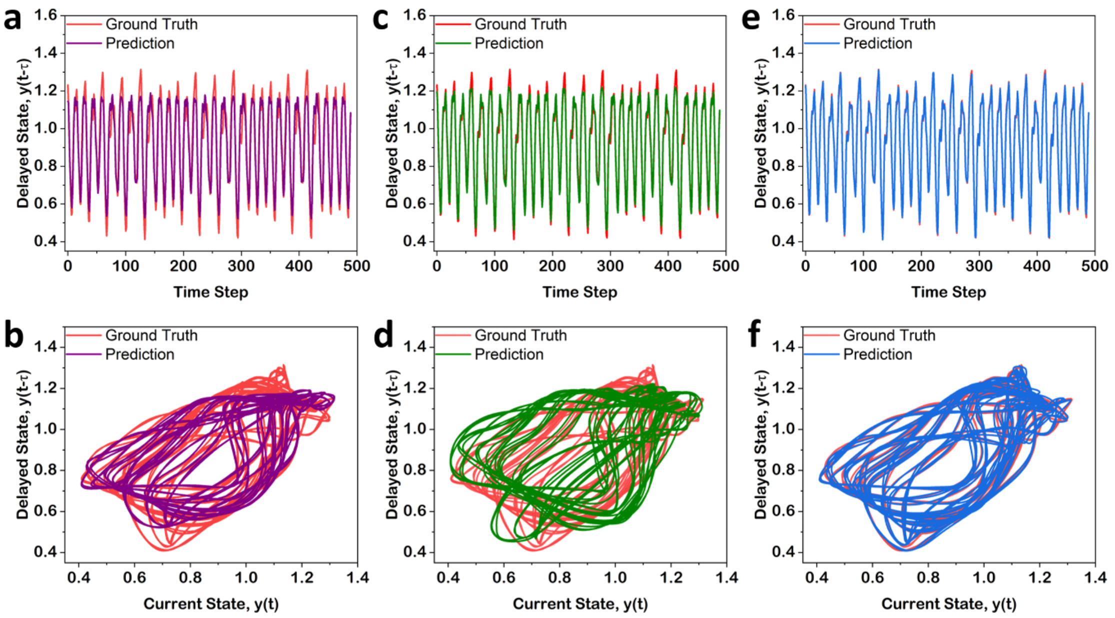

Figure 6. Comparison of MG prediction with the ground truth data in time domain based on the memristor time constant value τ of (a) 0.001 443 ms, (b) 0.014 43 ms, and (c) 1.443 ms, respectively. $\tau = 0.001\,443$ ms. The corresponding ground truth and prediction in phase space based on τ of (d) 0.001 443 ms, (e) 0.014 43 ms, and (f) 1.443 ms, respectively.

4. Conclusion

In this work, we demonstrated a Pt/TiO$_x$/Au memristor-based RC system capable of performing both image classification and chaotic time-series prediction by leveraging the device's inherent short-term plasticity and volatility. Using pulse modulation and natural relaxation, we achieved stable MNIST classification accuracy across multiple read timings under ideal conditions. However, performance degraded significantly with input variability and delayed readout, emphasizing the importance of early measurement to preserve state separability. A virtual memristor model, informed by experimental data, was employed to predict MG dynamics, showing increased accuracy from 72.2% to 93.6% as the internal time constant was extended.

Selection of the readout timing is critical in volatile memristor RC systems, as it directly relates to the relaxation dynamics of the memristors. Fast-relaxation memristors require prompt readouts post-pulse to capture encoded information accurately, while gradual-relaxation memristors offer a longer measurement window, supporting robust readouts in complex systems requiring precise input-output synchronisation. Simpler systems may benefit from fast relaxation memristors for rapid, accurate responses. These findings highlight the critical role of timing and variability in volatile memristor-based RC systems and suggest that future improvements could come from higher-resolution temporal sampling and heterogeneous reservoir architectures to enhance robustness and adaptability for complex tasks.

Data availability statement

The data that support the findings of this study are openly available at the following URL/DOI: doi.org/10.5258/SOTON/D3702.

Supporting Information Data available at https://doi.org/10.1088/1361-6463/ae23de/data1.

Acknowledgments

This work was supported by UKRI—Machine Intelligence for Nano-Electronic Devices and Systems (MINDS) [Grant number: EP/S024298/1], Marie Skłodowska-Curie Actions—European Commission [Grant No. 101029535-MENESIS] and The UK Royal Society [RG/R2/232206- SiMSANeC].

Conflict of interest

The authors declare no conflict of interest.

ORCID iDs

Alexander-Hanyu Wang 0000-0002-9572-0646
Omesh Kapur 0000-0001-8791-0899
Ruomeng Huang 0000-0003-1185-635X
Firman Simanjuntak 0000-0002-9508-5849

References

[1] Shi T *et al* 2025 Memristor-based feature learning for pattern classification *Nat. Commun.* **16** 913

[2] Wu X, Dang B, Zhang T, Wu X and Yang Y 2024 Spatiotemporal audio feature extraction with dynamic memristor-based time-surface neurons *Sci. Adv.* **10** eadl2767

[3] Yu Y, Xiao M, Fieser D, Zhoua W and Hu A 2024 Nanoscale memristor devices: materials, fabrication, and artificial intelligence *J. Mater. Chem. C* **12** 3770–810

[4] Zyarah A and Kudithipudi D 2024 Time-series forecasting and sequence learning using memristor-based reservoir system *ACM Trans. Embedded Comput. Syst.* **24** 1–17

[5] Bolón-Canedo V, Morán-Fernández L, Cancela B and Alonso-Betanzos A 2024 A review of green artificial intelligence: towards a more sustainable future *Neurocomputing* **599** 128096

[6] Barbierato E and Gatti A 2024 Toward green AI: a methodological survey of the scientific literature *IEEE Access* **12** 23989–4013

[7] Duan X, Cao Z, Gao K, Yan W, Sun S, Zhou G, Wu Z, Ren F and Sun B 2024 Memristor-based neuromorphic chips *Adv. Mater.* **36** 2310704

[8] Mehonic A and Kenyon A J 2022 Brain-inspired computing needs a master plan *Nature* **604** 255–60

[9] Singh A, Choi S, Wang G, Daimari M and Lee B-G 2025 Analysis and fully memristor-based reservoir computing for temporal data classification *Neural Netw.* **182** 106925

[10] Ju D, Noh M, Kim G, Park Y, Lee S and Kim S 2024 Reservoir computing system with diverse input patterns in HfAlO-based ferroelectric memristor *ACS Appl. Mater. Interfaces* **16** 66250–61

[11] Kleyko D, Kymn C J, Thomas A, Olshausen B A, Sommer F T and Frady E P 2025 Principled neuromorphic reservoir computing *Nat. Commun.* **16** 640

[12] Jiang S *et al* 2024 Energy-efficient reservoir computing based on solution-processed electrolyte/ferroelectric memcapacitive synapses for biosignal classification *J. Phys. Chem. Lett.* **15** 8501–9

[13] Wang X and Li H 2024 Reservoir computing with a random memristor crossbar array *Nanotechnology* **35** 415205

[14] Jere S, Zheng L, Said K and Liu L 2024 Universal approximation of linear time-invariant (LTI) systems through RNNs: power of randomness in reservoir computing *IEEE J. Sel. Top. Signal Process.* **18** 184–98

[15] Sakemi Y, Nobukawa S, Matsuki T, Morie T and Aihara K 2024 Learning reservoir dynamics with temporal self-modulation *Commun. Phys.* **7** 29

[16] Armendarez N, Hasan M S and Najem J 2024 Nonlinear memristor model with exact solution allows for ex situ reservoir computing training and *in situ* inference *Nanoscale* **17** 2068–77

[17] Peng H, Xiong X, Wu M, Wang J, Yang Q, Orellana-Martín D and Pérez-Jiménez M J 2024 Reservoir computing models based on spiking neural P systems for time series classification *Neural Netw.* **169** 274–81

[18] Lian M *et al* 2024 Towards mixed physical node reservoir computing: light-emitting synaptic reservoir system with dual photoelectric output *Light Sci. Appl.* **13** 179

[19] Chen R *et al* 2024 Thin-film transistor for temporal self-adaptive reservoir computing with closed-loop architecture *Sci. Adv.* **10** eadl1299

[20] Marrows C H, Barker J, Moore T A and Moorsom T 2024 Neuromorphic computing with spintronics *npj Spintronics* **2** 12

[21] Ju D, Noh M, Lee S, Kim G, Park J and Kim S Self-rectifying volatile memristor for highly dynamic functions *Adv. Funct. Mater.* **35** 2423880

[22] Ju D, Koo M and Kim S 2024 Implementation of 8-bit reservoir computing through volatile ZrO_x-based memristor as a physical reservoir *Nano Energy* **128** 109958

[23] Dutta M, Brivio S and Spiga S 2024 Unraveling the roles of switching and relaxation times in volatile electrochemical memristors to mimic neuromorphic dynamical features *Adv. Electron. Mater.* **10** 2400221

[24] Lee D K *et al* 2025 Crystallinity-controlled volatility tuning of ZrO memristor for physical reservoir computing *InfoMat* **7** e12635

[25] Kim J-H, Lee H J, Kim H-J, Choi J, Oh J-H, Choi D-C, Byun J, Ahn S-E and Lee S-N 2024 Oxide semiconductor memristor-based optoelectronic synaptic devices with quaternary memory storage *Adv. Electron. Mater.* **10** 2300863

[26] Jaafar A H, Shao L, Dai P, Zhang T, Han Y, Beanland R, Kemp N T, Bartlett P N, Hector A L and Huang R 2022 3D-structured mesoporous silica memristors for neuromorphic switching and reservoir computing *Nanoscale* **14** 17170–81

[27] Guo D, Kapur O, Dai P, Han Y, Beanland R, Jiang L, de Groot C H (Kees) and Huang R 2023 Reservoir computing using back-end-of-line SiC-based memristors *Mater. Adv.* **4** 5305–13

[28] Noh M, Park H and Kim S 2025 Dynamic resistive switching of WO_x-based memristor for associative learning activities, on-receptor, and reservoir computing *Chaos Soliton Fract.* **196** 116381

[29] Byun Y, So H and Kim S 2024 Convolutional neural network for high-performance reservoir computing using dynamic memristors *Chaos Soliton Fract.* **188** 115536

[30] Ye Z *et al* 2024 Self-rectifying TiO_x-based memristor with synaptic plasticity *J. Mater. Sci., Mater. Electron.* **35** 1223

[31] Park M H, Jeong J H, Kim W, Park S, Lim B M, Lee H-S and Kang S J 2024 A facile solution processible self-rectifying and sub-1 V operating memristor via oxygen vacancy gradient within a TiO_2 single layer *J. Mater. Chem. C* **12** 6881–92

[32] Yang T J *et al* 2024 Improvement of the symmetry and linearity of synaptic weight update by combining the InGaZnO synaptic transistor and memristor *IEEE Access* **12** 28531–7

[33] So H, Lee J, Mahata C, Kim S and Kim S 2024 Synaptic properties and short-term memory dynamics of TiO_2/WO_x heterojunction memristor for reservoir computing *Adv. Mater. Technol.* **9** 2301390

[34] Ju D, Lee J, So H and Kim S 2024 $TiN/TiO_x/WO_x/Pt$ heterojunction memristor for sensory and neuromorphic computing *J. Alloys Compd.* **1004** 175830

[35] Wang W, Wang Y, Yin F, Niu H, Shin Y-K, Li Y, Kim E-S and Kim N-Y 2024 Tailoring classical conditioning behavior in TiO_2 nanowires: znO QDs-based optoelectronic memristors for neuromorphic hardware *Nano-Micro Lett.* **16** 133

[36] Yu Y, Wang C, Jiang C, Wang L, Wang Z, Du Z, Sun J, Abrahams I and Huang X 2021 Nitrogen-doped titanium dioxide nanorod array memristors with synaptic features and tunable memory lifetime for neuromorphic computing *J. Alloys Compd.* **868** 159194

[37] So H, Ji H, Kim S and Kim S 2024 Sophisticated conductance control and multiple synapse functions in TiO_2-based multistack-layer crossbar array memristor for high-performance neuromorphic systems *Adv. Funct. Mater.* **34** 2405544

[38] Li Z *et al* 2025 Photoelectric reservoir computing based on TiO_x memristor for analog signal processing *ACS Appl. Nano Mater.* **8** 6591–603

[39] Yang C, Wang H, Cao Z, Chen X, Zhou G, Zhao H, Wu Z, Zhao Y and Sun B 2024 Memristor-based bionic tactile devices: opening the door for next-generation artificial intelligence *Small* **20**

[40] Zhong Y *et al* 2022 A memristor-based analogue reservoir computing system for real-time and power-efficient signal processing *Nat. Electron.* **5** 672–81

[41] Taj I and Farooq U 2023 Towards machine learning-based FPGA backend flow: challenges and opportunities *Electronics* **12** 935

[42] Li R, Yang H, Zhang Y, Tang N, Chen R, Zhou Z, Liu L, Kang J and Huang P 2023 Adjustable short-term memory of SiO_x:Ag-based memristor for reservoir computing *Nanotechnology* **34** 505207

[43] Jaurigue L and Lüdge K 2024 Reducing reservoir computer hyperparameter dependence by external timescale tailoring *Neuromorphic Comput. Eng.* **4** 014001

[44] Khalid A, Ahmad P, Alharthi A I, Muhammad S, Khandaker M U, Iqbal Faruque M R, Din I U and Alotaibi M A 2021 Unmodified titanium dioxide nanoparticles as a potential contrast agent in photon emission computed tomography *Crystals* **11** 171

[45] Wang L, Cheng B, Zhang L and Yu J 2021 In situ irradiated XPS investigation on S-scheme TiO_2@$ZnIn_2S_4$ photocatalyst for efficient photocatalytic CO_2 reduction *Small* **17** 2103447

[46] Vargas-Villanueva S, Torres-Ceron D A, Amaya-Roncancio S, Arellano-Ramírez I D, Riva J S and Restrepo-Parra E 2022 Study of the incorporation of S in $TiO_2/SO_4{}^{2-}$ coatings produced by PEO process through XPS and DFT *Appl. Surf. Sci.* **599** 153811

[47] Hernández-Arriaga H, López-Luna E, Martínez-Guerra E, Turrubiartes M M, Rodríguez A G and Vidal M A 2017 Growth of HfO_2/TiO_2 nanolaminates by atomic layer deposition and HfO_2-TiO_2 by atomic partial layer deposition *J. Appl. Phys.* **121** 064302

[48] Torres-Ceron D A, Amaya-Roncancio S, Riva J S, Vargas-Eudor A, Escobar-Rincon D and Restrepo-Parra E 2021 Incorporation of P^{5+} and P^{3-} from phosphate precursor in TiO_2:P coatings produced by PEO process: XPS and DFT study *Surf. Coat. Technol.* **421** 127437

[49] Moon T, Soh K, Kim J S, Kim J E, Chun S Y, Cho K, Yang J J and Yoon J H 2024 Leveraging volatile memristors in neuromorphic computing: from materials to system implementation *Mater. Horiz.* **11** 4840–66

[50] Wang K, Lu J, Xiang Z, Shi M, Wu L, Yan F and Jiang R 2024 Investigation of the adaptability of Pt/HfO_2/n^+Si memristors with self-limiting oxygen-deficient hafnium oxide films under repetitive pulse stimuli *Adv. Phys. Res.* **3** 2400047

[51] She Y, Wang F, Zhao X, Zhang Z, Li C, Pan H, Hu K, Song Z and Zhang K 2021 Oxygen vacancy-dependent synaptic dynamic behavior of TiO_x-based transparent memristor *IEEE Trans. Electron Dev.* **68** 1950–5

[52] Li Z *et al* 2024 Crossmodal sensory neurons based on high-performance flexible memristors for human-machine in-sensor computing system *Nat. Commun.* **15** 7275

[53] Hu J, Li B, Wang H, Kang Y, Zhao Y, Xu Y, Shi E, Guo Y, Xu K and Yu B 2025 Self-compliant, variation-suppressed memristor implemented with carbon nanotube/hBN/silver nanowire cross-point structure *Adv. Funct. Mater.* **35** 2424131

[54] Li Z, Wang J, Xu L, Wang L, Shang H, Ying H, Zhao Y, Wen L, Guo C and Zheng X 2024 Achieving reliable and ultrafast memristors via artificial filaments in silk fibroin *Adv. Mater.* **36** 2308843

[55] Zhuang P *et al* 2023 Large-area multilayer molybdenum disulfide for 2D memristors *Mater. Today Nano* **23** 100353

[56] Kim M *et al* 2024 Study on the sodium-doped titania interface-type memristor *ACS Appl. Mater. Interfaces* **16** 16453–61

[57] Zhang T, Shao L, Jaafar A, Zeimpekis I, de Groot C H, Bartlett P N, Hector A L and Huang R 2024 Tunable neuromorphic switching dynamics via porosity control in mesoporous silica diffusive memristors *ACS Appl. Mater. Interfaces* **16** 16641–52

[58] Jang Y H, Lee S H, Han J, Kim W, Shim S K, Cheong S, Woo K S, Han J-K and Hwang C S 2024 Spatiotemporal data processing with memristor crossbar-array-based graph reservoir *Adv. Mater.* **36** 2309314

[59] Lu Z-N, Ye J-T, Zhang Z-D, Cai J-W, Pan X-Y, Xu J-L, Gao X, Zhong Y-N and Wang S-D 2024 Memristor-based input delay reservoir computing system for temporal signal prediction *Microelectron. Eng.* **293** 112240